RESEARCH ARTICLE | JUNE 11 2024

Physical aspects of vortex-shock dynamics in delta wing configurations $\ensuremath{ igoplus }$

K. Rajkumar 🗷 📵 ; T. Di Fabbio 📵 ; E. Tangermann; M. Klein 🗓



Physics of Fluids 36, 066112 (2024) https://doi.org/10.1063/5.0213122





Articles You May Be Interested In

Mechanism of periodic oscillation in low-Reynolds-number buffet around an airfoil at angle of attack 0 Physics of Fluids (April 2024)

Adaptive control of transonic buffet and buffeting flow with deep reinforcement learning Physics of Fluids (January 2024)

Mitigation of transonic shock buffet on a supercritical airfoil through wavy leading edges

Physics of Fluids (February 2021)



Physics of Fluids

Special Topics Open for Submissions

Learn More



Physical aspects of vortex-shock dynamics in delta wing configurations

Cite as: Phys. Fluids **36**, 066112 (2024); doi: 10.1063/5.0213122 Submitted: 8 April 2024 · Accepted: 18 May 2024 · Published Online: 11 June 2024











K. Rajkumar, and M. Klein 🕞 E. Tangermann, and M. Klein 🕞

AFFILIATIONS

Department of Aerospace Engineering, Institute of Applied Mathematics and Scientific Computing, University of the Bundeswehr Munich, Neubiberg 85579, Germany

^{a)}Author to whom correspondence should be addressed: karthick.rajkumar@unibw.de

ABSTRACT

Delta wing configurations with double- and triple-leading edges introduced within the North Atlantic Treaty Organization Applied Vehicle Technology -316 task group are examined to investigate the dynamics of vortices and shocks, with potential implications for the preliminary aircraft design. The numerical simulations are conducted for the configurations at $Ma_{\infty}=0.85$ and $Re_{\infty}=12.53\times10^6$ using the Reynoldsaveraged Navier-Stokes $k-\omega$ shear stress transport (SST) model across a range of incidence angles. The detailed analysis focuses on the case with $\alpha=20^\circ$ using the scale-adaptive simulation based on the $k-\omega$ SST model. This study considers shock-vortex interaction and breakdown with buffeting to study the transient flow physics over the wing. Additionally, insights into vorticity strength and destruction are gained through the enstrophy transport equation. The findings reveal that the inboard vortex (IBV) development is impeded by counter-rotating secondary vortices from IBV and the midboard vortex. A key distinction is observed for the first time between the double-delta and triple-delta wings, in that the double-delta wing experiences shock-induced vortex breakdown, with the transient nature of this breakdown leading to an adjustment in the shock position, causing a shock buffet. In contrast, the breakdown in the triple-delta wing is linked to a stationary shock induced by the kink in the planform. This study highlights the crucial role of the orientation of the shock relative to the vortex axis in characterizing the aerodynamic performance of the planforms.

Published under an exclusive license by AIP Publishing. https://doi.org/10.1063/5.0213122

I. INTRODUCTION

Highly agile, high-performance aircraft configurations must meet diverse performance and maneuverability demands. These requirements have led to the development of various aircraft configurations, including double-delta, strake trapezoidal, or canard delta wings. These designs exploit controlled vortex flows over the wings to achieve high lift and maneuverability. Predominantly featured in combat aircraft, these configurations offer aerodynamic advantages that enhance overall performance and capabilities. Swept leading edges in delta wings improve maneuverability at high speeds, a critical feature for combat aircraft to maintain control. Different types of combat aircraft, such as interceptors, multi-role fighters, and stealth aircraft, may employ slightly different wing sweep angles to optimize performance for their designated roles.

In delta wing planforms, the flow is dominated by counterrotating leading-edge vortices. Under subsonic conditions, as the angle of incidence increases, the vortex breaks down due to the rising adverse pressure gradient within the flow. This breakdown causes adverse roll at sideslip and eventual loss of directional stability.² In transonic flow conditions, shocks further complicate the dynamics of the vortex system and its breakdown characteristics. The sudden breakdown of the vortex can significantly impact the aerodynamic behavior of the wing. The vortex breakdown exhibits asymmetry in conditions involving sideslip, with the breakdown point positioned further upstream on the windward side compared to the leeward side, as discussed in Ref. 3. These characteristics are responsible for typical longitudinal, lateral, and directional instabilities, such as pitch-up, roll reversal, and directional divergence. These instabilities have been observed in generic low-aspect-ratio wing/body configurations and various high-performance aircraft designs. Addressing or eliminating these instabilities could potentially expand the operational flight envelope of such configurations.⁴

One approach to address aerodynamic instabilities is manipulating the leading-edge vortex by creating a system of multiple interconnected leading-edge vortices. It can be achieved through the design of the wing planform. By carefully varying the leading-edge sweep along

the wing span, it is possible to stimulate the formation of more than one leading-edge vortex. The proximity of these vortices leads to their interaction, which, in turn, affects their characteristics. This interaction aims to induce a stabilizing influence on the vortex system, ultimately enhancing overall aerodynamic stability. However, effectively harnessing vortex interaction necessitates a thorough understanding of the underlying flow physics.

In transonic flow conditions, the breakdown position suddenly moves toward the apex as the angle of incidence increases. It was observed by Schiavetta *et al.*⁵ over a 65° sharp edge delta wing. They determined that the shock/vortex interaction was the cause of the sudden motion, and the presence and effect of this interaction were studied in terms of the Rossby number of the vortex and the axial flow properties. Furthermore, they found that the movement of the breakdown location is sensitive to the balance among vortex strength, axial flow, and shock strength. However, in the context of shock interaction with the vortex system, more emphasis must be placed on the unsteady aspects of these vortical flows, which impact aircraft stability and control.⁶ For instance, shock-induced vortex breakdown is a transient phenomenon. It has a direct impact on the pitching moment. Understanding its mechanism better controls the longitudinal stability of the aircraft and ensures high maneuverability.

In an attempt to determine the underlying theory behind vortex breakdown, numerous studies have been undertaken, primarily focusing on simple geometries such as torsionally driven cylinders and closed pipes. This research investigation has been gaining interest since Peckham and Atkinson⁷ first observed this phenomenon over a delta wing planform. In the context of straightforward geometric configurations, the breakdown phenomenon of an axisymmetric vortex is linked to the localized trapping and amplification of disturbances within the vortex core. Nevertheless, some researchers have raised doubts about whether the phenomenon observed in torsionally driven cylinders should be classified in the same category as that occurring over delta wings, as articulated by Darmofal and Murman in 1994.⁸

Despite significant advances in developing the fundamental theory of vortex breakdown, this understanding has yet to yield universally effective control measures. Current control strategies rely on manipulating the vortex swirl ratio or the pressure gradient above the wing. Whereas these methods exhibit varying degrees of effectiveness, they do not leverage an understanding of the breakdown mechanism. A noteworthy contribution by Rusak and Lamb demonstrated that the swirl ratio (defined as the ratio of the maximum azimuthal velocity to the maximum axial velocity within the vortex), previously utilized to indicate the susceptibility of flow to breakdown in open pipes, could be employed to predict the onset and location of breakdown over slender delta wings.

A study by Jones *et al.*¹¹ successfully confirmed the vorticity dynamics linked to vortex breakdown above a delta wing with less complex geometries. Additionally, the study demonstrated that the presence of negative azimuthal vorticity serves as an indicator for the initiation of vortex breakdown. Moreover, the investigation delved into the mechanism responsible for generating this negative azimuthal vorticity. It highlighted the role of radial vorticity, which opposes the onset of breakdown, and the turning of axial vorticity into the azimuthal direction appears to be the main contributor to the onset of vortex breakdown.

A research initiative focused on investigating vortex interaction effects was led by Airbus Defence and Space (ADS), in collaboration

with the German Aerospace Center (DLR). Double and triple-delta wing planforms, referred to as DW1 and DW2 in this study, were defined within this initiative. The configuration under examination entails a generic low-aspect-ratio wing-fuselage setup, with active participation in the North Atlantic Treaty Organization (NATO) Applied Vehicle Technology (AVT)-316 task group titled "Vortex Interaction Effects Relevant to Military Air Vehicle Performance." 12-14 Several studies have been undertaken to study these configurations over a range of subsonic and transonic Mach numbers. These planforms are especially significant for combat aircraft, as they frequently encounter high angle of attack situations, requiring designs that ensure stability and control even in extreme flight conditions. The investigations encompass alterations in geometry and flow conditions, with distinct wing sweep angles significantly amplifying flow intricacy. The geometric disparity at the leading edge results in the generation of vortices, each exhibiting differences in strength, stability, and characteristics influenced by the sweep angles of their origin. Moreover, these vortices interact or combine in diverse manners contingent upon the angles of attack and sideslip.

Hövelmann et al.¹⁵ conducted a joint experimental and numerical investigation employing URANS computations to analyze the aerodynamics of a generic triple-delta wing configuration at transonic velocities. The primary focus was comprehending vortex flow phenomena, encompassing vortex development, vortex–vortex, and vortex–shock interactions. The research outcomes encompassed flow conditions at Mach numbers of 0.5 and 0.85, encompassing various angles of attack (up to 40°) and non-symmetric flows, including non-null sideslip angles. The findings indicate that the experimental and computational results generally concur at lower to medium angles of attack. However, discrepancies arise as the angle of attack increases, particularly concerning predicting vortex breakdown effects. These disparities are more evident in lateral motion scenarios, where experimental and numerical results highlight differing predictions of vortex breakdown effects.

Pfnür and Breitsamter¹⁸ studied the double and triple delta wing planforms in subsonic flow conditions, focusing on investigating the interactions between inboard and midboard vortex structures, as well as analyzing the properties and trajectories of these vortices. The study revealed that the breakdown behavior associated with distinct vortex types exerted varying effects on the stability of the midboard vortex. Notably, both planforms exhibited significant instabilities in the medium to high angle-of-attack regimes, but their onset and magnitude were notably reduced for the triple-delta wing configuration.

A previous study by Di Fabbio $et~al.^{19}$ simulated the triple-delta wing planform and compared the performance of different turbulence approaches by analyzing different chord-wise locations and local surface pressure distribution. We showcased the capability of $k-\omega$ shear stress transport (SST) and scale-adaptive simulation (SAS) models to predict the aerodynamic coefficients more effectively than RANS (Reynolds-averaged Navier–Stokes) models such as SA-negRC. This study mainly focuses on the investigations of physical aspects of vortex dynamics responsible for the distribution of local surface pressure. This study simulates the flow around the double-delta wing DW1 using the $k-\omega$ SST RANS model and the SAS turbulence modeling approach to analyze the transient flow characteristics occurring over the wing. In this context, the flow fields over planforms have been investigated in the transonic regime at $Ma_\infty=0.85$ and

 $Re_{\infty}=12.53\times10^6$ with $\beta=5^\circ$. In particular, the flow physics, such as vortex–vortex interaction, vortex–shock interactions, and shock-buffet of both the planforms will be addressed. The evolution of lambda-shock and its buffet will be addressed for the first time. Moreover, several conclusions could be drawn to the vortex dynamics based on the different sweep angles of the leading edges. Vorticity transport terms reveal the physical mechanisms relating to vortex strength, and the position and orientation of the shock have been discussed, highlighting their potential significance in aircraft design.

II. COMPUTATIONAL APPROACH

A. Model configurations and computational mesh

Figure 1 displays planform sketches of DW1 and DW2 configurations. These are 1:30-scaled versions of a generic fuselage and a flatplate wing with a sharp leading edge featuring same chord length c_r . DW1 features a double-delta wing planform with two different leading-edge sections, while DW2 is designed with a triple-delta wing planform.²⁰ The wing configuration includes flat-plate wings with sharp leading edges and control surfaces, namely levcon, slat, and flaps. Both planforms have a leading-edge sweep angle of $\phi_3 = 52.5^{\circ}$ for the outer wing section. In DW2, the strake section exhibits two different angles of $\phi_1 = 52.5^{\circ}$ and $\phi_2 = 75^{\circ}$, whereas DW1 features one highly swept strake with an angle of $\phi_2 = 75^\circ$. Nautical labeling will be employed, with "starboard" indicating (y > 0) and "portside" indicating (y < 0). In sideslip flow, the portside is located windward, and the starboard is leeward. The geometrical parameters of the planforms have been listed in Table I, with more details about the wing configuration can be found in Ref. 15.

The meshing strategy for DW1 is followed based on previous studies by Di Fabbio *et al.*²⁰ for DW2 configuration. The numerical mesh employed for both planforms is of the unstructured type. The walls' surfaces are composed of triangles. Prism grids exhibit more excellent orthogonality, reducing computational effort while maintaining good solution accuracy. To resolve the boundary layer over the flat-plate planforms, up to 35 layers of triangular prism elements are utilized for the surface elements, with the first cell height $y^+ \approx 1$. Flow features, such as the shear layer and resulting vortices, extend in and

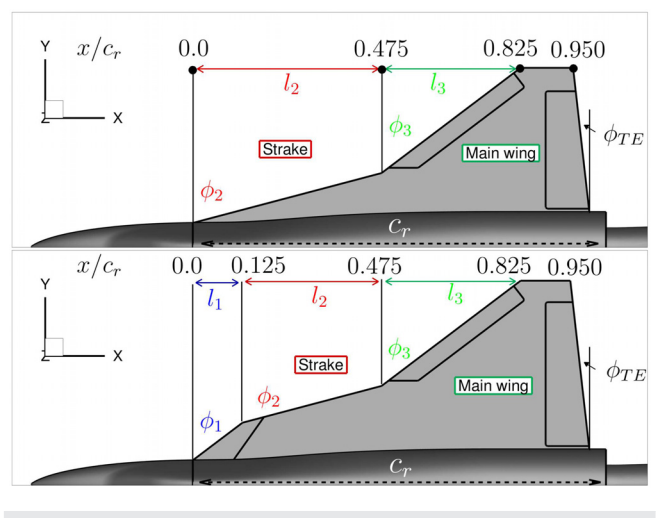


FIG. 1. Planforms DW1 and DW2.

TABLE I. Geometrical parameters of DW1 and DW2.

	DW1	DW2
l_1/c_r		0.125
$l_1/c_r \ l_2/c_r$	0.475	0.350
l_3/c_r	0.350	0.350
ϕ_1		52.5°
ϕ_2	75°	75°
ϕ_3	52.5°	52.5°

out of the boundary between the prism and tetrahedral mesh. Other regions of the spherical computational domain, with a diameter of $50c_r$, consist of unstructured elements comprising tetrahedral and pyramid cells. The model has been meshed in half and mirrored about the symmetry axis to avoid asymmetric grid effects. Isotropic mesh refinement has been applied in the vortex regions. A mesh convergence study (refer to Sec. III A) has been conducted, and the resulting mesh has been used for the URANS simulation. In the case of SAS, local regions within and around the configuration have been refined based on scale estimates obtained from the $k-\omega$ SST model. 2–3 cells per integral length scale have been employed to resolve the vortex and surrounding regions. Figure 2 illustrates the SAS's resulting surface and volume mesh distribution, with cells clustered in the boundary layer and around the vortex region. The configurations feature viscous noslip walls, and the domain has far field flow conditions with an undisturbed flow within the surrounding sphere.

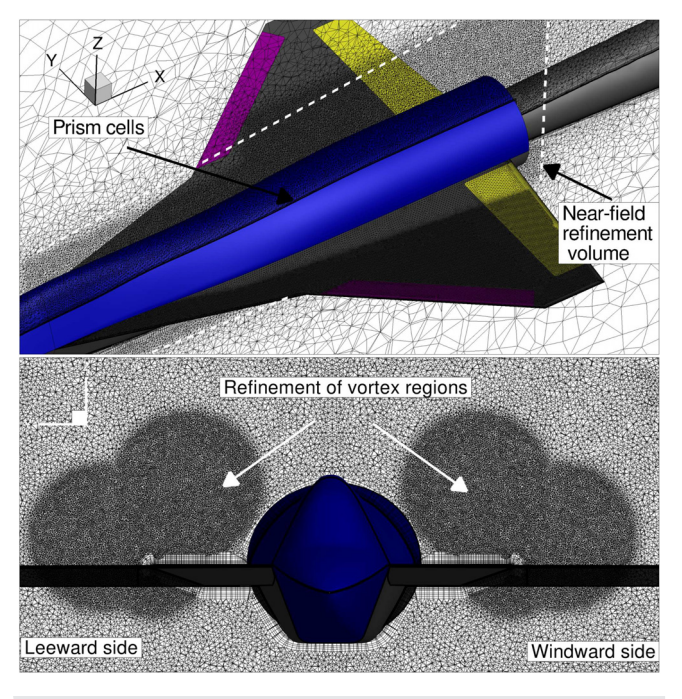


FIG. 2. DW1 mesh topology showing surface mesh distribution (top) and volume cells distribution at $x/c_r = 0.4$ (bottom).

B. Numerical setup

This study uses a three-dimensional, parallel, hybrid, finite volume code developed by the German Aerospace Center, DLR-TAU, to carry out the numerical simulations using the compressible Navier–Stokes equations. Reader is to referred to the work of Langer *et al.* ²¹ for more details on the code and its validation. Compared to the Navier–Stokes equations, additional terms arise from the Reynolds averaging of non-linear terms, constituting new unknowns that need to be modeled. These are, in particular, the components of the so-called Reynolds stress tensor τ_{ij} , which are given by the Boussinesq assumption as follows:

$$\tau_{ij} = \mu_t \left(2S_{ij} - \frac{2}{3} \frac{\partial u_k}{\partial x_k} \delta_{ij} \right) - \frac{2}{3} \rho k \delta_{ij}, \tag{1}$$

where $S_{ij} = \frac{1}{2} \left(\frac{\partial u_i}{\partial x_j} + \frac{\partial u_j}{\partial x_i} \right)$ is the strain rate tensor. For convenience, we have omitted the overbars denoting averaged quantities.

The $k-\omega$ SST model has been employed in this study, where two transport equations for turbulent kinetic energy k [Eq. (2)] and specific rate of dissipation ω [Eq. (3)] are solved to model the contribution of the turbulence to the momentum equations²²

$$\frac{\partial \rho k}{\partial t} + u_i \frac{\partial \rho k}{\partial x_i} = P_{k\omega} - \beta^* \rho \omega k + \frac{\partial}{\partial x_j} \left[(\mu + \sigma_{k1} \mu_t) \frac{\partial k}{\partial x_j} \right], \quad (2)$$

$$\frac{\partial \rho \omega}{\partial t} + u_i \frac{\partial \rho \omega}{\partial x_i} = \frac{\gamma_1}{\nu_t} P_{k\omega} - \beta_1 \rho \omega^2 + \frac{\partial}{\partial x_j} \left[(\mu + \sigma_{\omega 1} \mu_t) \frac{\partial \omega}{\partial x_j} \right]. \quad (3)$$

The turbulence production term $P_{k\omega}$ is defined by $\tau_{ij} \frac{\partial u_i}{\partial x_j}$. The SAS approach applied to a RANS model compares the turbulence length scale and the von Karman length scale. The information allows the SAS model to dynamically adjust to resolved structures in a RANS simulation, which results in an LES-like behavior in unsteady regions of the flowfield. At the same time, the model provides standard RANS capabilities in steady flow regions. According to Menter et $al.,^{23}$ the model has been used in this study. This scale-resolving technique has been used here with the standard $k-\omega$ SST model 22 as the base model. The governing equations of the SST-SAS model differ from the $k-\omega$ SST model by the additional source term Q_{SAS} in the transport equation for ω , which is defined as shown in the below equation:

$$\begin{aligned} Q_{SAS} &= max \left[\rho \zeta_2 S^2 \left(\frac{L}{L_{vK}} \right)^2 \right. \\ &\left. - F_{SAS} \frac{2\rho k}{\sigma_{\phi}} max \left(\frac{1}{k^2} \frac{\partial k}{\partial x_j} \frac{\partial k}{\partial x_j}, \frac{1}{\omega^2} \frac{\partial \omega}{\partial x_j} \frac{\partial \omega}{\partial x_j} \right), 0 \right]. \end{aligned} \tag{4}$$

TABLE II. Details of meshes A-E for mesh refinement study in URANS (DW1).

Mesh A Mesh B Mesh C Mesh D Mesh E 2.8×10^{6} 82.2×10^{6} No. of mesh nodes 4.8×10^{6} 10.4×10^{6} 27.3×10^{6} y^+ of the first element 1.0 1.0 1.0 1.0 1.0 Number of prism cells 35 35 35 35 35 Resolution in $0.0006C_{r}$ $0.0042C_{r}$ $0.0028C_{r}$ $0.0018C_{r}$ $0.0012C_{r}$ vortex regions

The von Karman length scale $L_{\nu K}$ given by

$$L_{\nu K} = \kappa \frac{u'}{|u''|}; \quad u'' = \sqrt{\frac{\partial^2 u_i}{\partial x_k^2} \frac{\partial^2 u_i}{\partial x_i^2}}; \quad u' = \sqrt{2 \cdot S_{ij} S_{ij}},$$

with k = 0.41, $\zeta_2 = 1.755$, $\sigma_{\phi} = 2/3$, and $F_{SAS} = 1.25$.

The simulations employed a second-order central scheme for spatial discretization with artificial dissipation schemes. Specifically, the convective mean-flow terms were treated with a skew-symmetric central scheme according to Kok.²⁴ In contrast, the convective terms of the turbulence equations were discretized with the central average of the analytic flux on each side of the face. A matrix artificial dissipation of 80% and a scalar artificial dissipation of 20% were set in the computations. The temporal discretization has been achieved through a dual-time stepping approach, which follows the approach of Jameson et al.25 A second-order implicit backward method with the LUSGS algorithm is employed for discretizing the time-derivative to generate a sequence of (non-linear) steady-state problems, which make use of the singly diagonally implicit Runge-Kutta method (SDIRK) until a steady state in fictitious pseudo time is reached. Further details regarding the DLR-TAU solver can be found in the study by Galle et al. 26 The surfaces of the delta wing configurations are treated as no-slip walls. Free-stream conditions Ma and Re are given as input to the solver. To match these nondimensional numbers, the reference temperature is prescribed based on wind tunnel data. Following this, the dynamic viscosity is computed from Sutherland's law,²⁷ and reference pressure is computed. These reference values are used in the computation of aerodynamic coefficients.

III. RESULTS AND DISCUSSION

A. Grid independence study

This section discusses the analysis to determine a suitable mesh for the DW1 planform. Given the transient nature of vortex breakdown and shock location, there might be more suitable solutions than a steady RANS simulation. Therefore, we opted for the URANS approach, specifically utilizing the $k-\omega$ SST model. For the study, we selected five meshes (labelled A-E) with progressively finer resolution in each direction within the vortex regions, featuring a growth factor of 1.5. According to widely accepted best practice guidelines for aerodynamic flows, a y⁺ value at the order of 1.0 should be used for wall resolved turbulence modeling.² According to Menter, 22 the SST turbulence model requires y^+ values smaller than 3, whereas Georgiadis et al.²⁹ reported grid independent solutions using grids with an average y^+ value between 1 and 2. In the present study, 35 prism layers combined with grid stretching have been utilized, with the first cell height set to 1×10^{-5} times the chord length to achieve $y^{+} \approx 1.0$. Meshes A-E have sizes of 2.8×10^{6} , 4.8×10^{6} , 10.4×10^{6} , 27.3×10^6 , and 82.2×10^6 nodes, respectively (see Table II). The

wall-normal resolution was consistent across all meshes, ensuring that the first cell's y^+ value remained below 1.0.

The aerodynamic coefficients predicted, including the lift coefficient $C_{L\nu}$ rolling moment coefficient $C_{m\nu}$ and pitching moment coefficient $C_{m\nu}$ from these meshes are illustrated in Fig. 3. The coefficients are defined as

$$C_L = rac{L}{q_{\infty} \mathcal{S}_{ref}}$$
 $C_{mx} = rac{M_x}{q_{\infty} \mathcal{S}_{ref} l_{ref}}$ $C_{my} = rac{M_y}{q_{\infty} \mathcal{S}_{ref} l_{ref}},$

where L denotes the lift force, while M_x and M_y represent the rolling and pitching moments, respectively. S_{ref} serves as the reference area, q_{∞} represents the freestream dynamic pressure, and l_{ref} is utilized as the reference length for the non-dimensionalization of aerodynamic forces and moments. The simulated physical time corresponds to approximately 38 convective time units (CTU), during which it is observed that meshes D and E converge to similar values of lift and moment coefficients. It is observed that as the mesh resolution increases, the oscillation frequency of the coefficients diminishes. Simulation results can be considered statistically stationary after 0.04s,

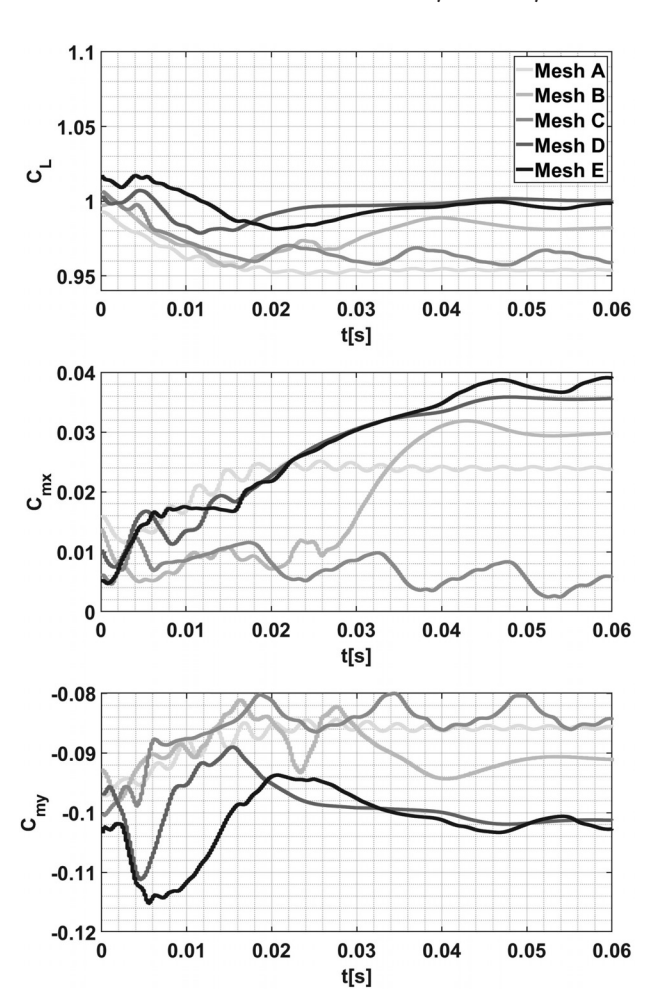


FIG. 3. Mesh convergence study at $\alpha=20^\circ$ and $\beta=5^\circ$ in DW1 using URANS $k-\omega$ SST model ($Ma_\infty=0.85$ and $Re_\infty=12.53\times10^6$).

providing more than 12 CTU for statistical averaging. The averaging time is similar to many aerodynamic flows, as demonstrated by studies.31-33 Figure 4 shows the relative deviation of the averaged aerodynamic coefficients for different meshes compared to the finest mesh E. The deviation is less than 2.0% for C_L and C_{my} and less than 6.0% for C_{mx} on mesh D, which is used for the production runs. A similar deviation is observed relative to the wind tunnel experiments (see Sec. III B). Such minor deviations are insignificant for the qualitative analysis presented in this work. Furthermore, based on our experience with flows involving vortex and shock interaction, which lead to eventual vortex breakdown, achieving ideal mesh convergence is challenging due to the oscillation of the breakdown location. This oscillation may explain the unexpected behavior observed in mesh C after local mesh refinement in the vortex-breakdown region. Based on these results, mesh D with 27.3×10^6 nodes was selected for the unsteady RANS simulation. In the SAS simulations, the vortex-core regions have ensured that 2-3 cells are placed to resolve integral length scales, resulting in a similar mesh as that of mesh D with around 30×10^6 nodes. Similar approaches for mesh independence have also been performed for DW2.

B. Performance of simulation methods

The computations have been performed for various incidence angles, as shown in Fig. 5. The lift coefficients are well-predicted for both planforms. However, the simulation for the DW2 planform does not predict the drop in lift by 18% between $\alpha=20^{\circ}$ and $\alpha=24^{\circ}$. Due to the asymmetric flow and vortex breakdown at high incidence angles, the moment coefficients exhibit more significant variations than the lift coefficient, making it challenging to discuss them to validate the simulation results.

The rolling moment plot demonstrates the accuracy of the simulation results for both planforms, which are in good agreement with the measurement data. The prediction for the DW1 planform is particularly accurate. The simulation captures an increase in approximately 1.3 times the coefficient for DW2. The simulation results capture the general trend of the pitching moment, although the absolute values slightly differ from the experimental data.

At $\alpha=20^\circ$, both planforms show significant differences in the aerodynamic characteristics due to shock and vortex breakdown. Therefore, this specific case has been analyzed in detail with SAS. It is important to note that, generally, SAS results at these incidence angles exhibit better accuracy than the $k-\omega$ SST model for both planforms.

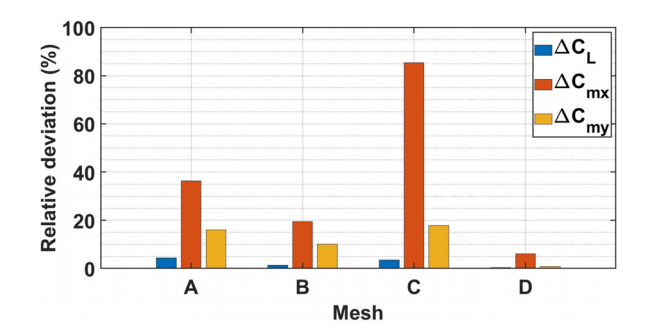


FIG. 4. Relative deviation of aerodynamic coefficients compared to mesh E.

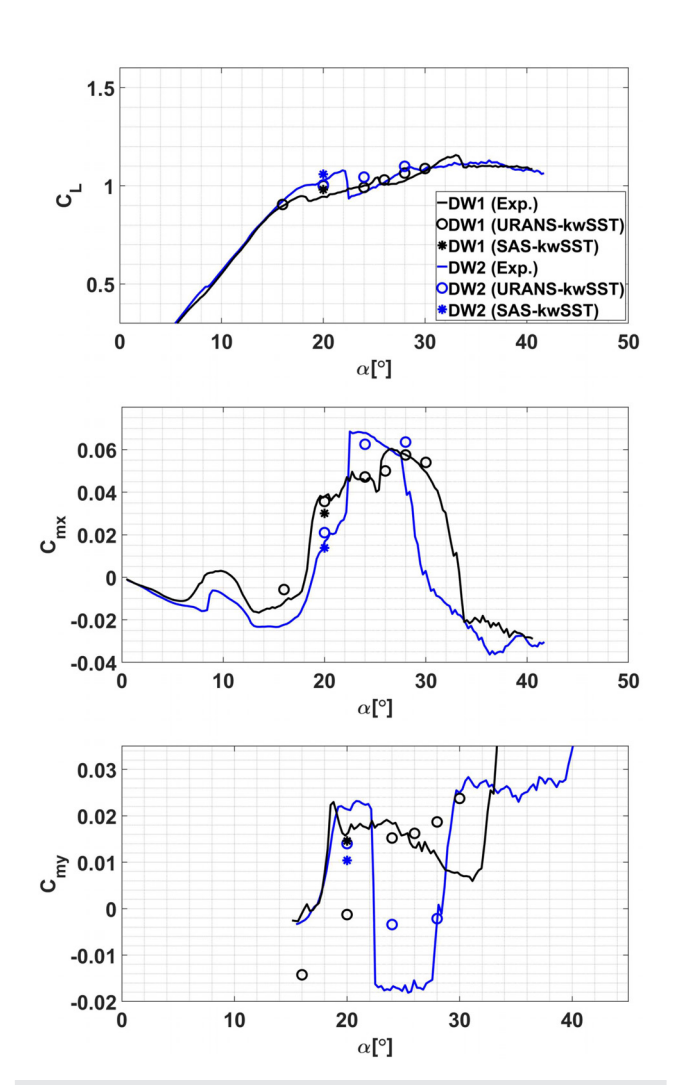


FIG. 5. Aerodynamic coefficients of DW1 and DW2—Experiment and simulation models, namely the $k-\omega$ SST and SAS model at $Ma_{\infty}=0.85$ and $Re=12.53\times 10^6$ with $AoS=5^{\circ}$.

C. Analysis of the vortex system

Reader is directed to the study conducted by Di Fabbio et al. 19 for a comprehensive comparison of surface mean- C_p values predicted by various turbulence models, including the $k - \omega$ SST and SAS models, against pressure-sensitive paint (PSP) measurement data. Figure 6 offers a detailed insight into the flow fields of DW1 and DW2, presenting transparent slices showcasing Q at varying angles of attack: 16° and 20°. At $\alpha = 16^{\circ}$ in DW1, the inboard vortex (IBV) originates on both sides of the wing from the highly swept leading edge section and progresses downstream. The IBV's trajectory straightens and diverges from the leading edge as the wing transitions to the medium-swept section. Concurrently, the shear layer separates from the mediumswept leading edge, forming an additional leading-edge vortex known as the midboard vortex (MBV). Both the IBV and MBV interact downstream, moving toward the trailing edge. In DW2, IBVs on either side develop from the levcon and highly swept leading edge. Generally, on the windward side, the fusion of the outboard vortex (OBV) with the MBV results in the MBV's dissolution, while on the leeward side, MBVs and OBVs interact and strengthen. At $\alpha=20^{\circ}$ in DW1, both windward and leeward IBVs enlarge compared to their counterparts at $\alpha=16^{\circ}$. On the windward side, the MBV exhibits significant spanwise motion, eventually rolling over the IBV, whereas on the leeward side, the MBV interacts with the IBV, supporting its existence. Notably, the windward IBV experiences breakdown, indicated by black dotted lines. In DW2, the IBV expands considerably upstream compared to DW1 due to shocks generated by the kink in its triple-delta wing planform. As a result of the IBV's burst, the subsequent MBV is diverted, preventing it from rolling over the IBV as observed in DW1. Generally, on the windward side, the MBV surpasses the IBV without interaction, while on the leeward side, the MBV interacts with the IBV, forming a stronger vortex system. The interaction between MBVs and outboard vortices OBVs is more noticeable at low-incidence angles. Conversely, the interaction between MBVs and inboard vortices (IBVs) becomes more pronounced at high-incidence angles.

Figure 7 showcases the vortex system at higher angles of attack, specifically 24° and 28° . At $\alpha=24^\circ$ in DW1, the windward IBV experiences upstream breakdown compared to the 20° case, with no presence of MBV and OBV observed, while the leeward MBV rises and expands in diameter. The OBV merges and interacts downstream with the IBV. No vortex is generated in DW2 on the windward side. Generally, a distinct unwrapping pattern becomes evident in the vortices, accompanied by increased vortex-core diameter as the incidence angle rises. Moreover, vortices produced over the main wing (MBV and OBVs) show diminishing presence in these high-incidence cases. Additionally, the flow field reveals the formation of two prominent fuselage vortices, particularly at 20° , 24° , and 28° .

It has been reported for incompressible flows that at very low incidence angles, the vortex-vortex interaction is weak, and an increase in the incidence angle makes the interaction stronger before it becomes unstable at very high angles of attack. As the angle of attack increases, the vortex starts to break down because of the stronger adverse pressure behind its core. As the angle of attack increases, the point where this breakdown happens moves further toward the front of the wing (see Fig. 6). In transonic flow conditions, the flow field shows sudden changes due to the presence of the shock. Moreover, the interactions of the two vortices are not only dependent on the state of the vortices but also on the position and orientation of the shocks in the transonic case,

$$\frac{\partial \omega_{i}}{\partial t} + u_{k} \frac{\partial \omega_{i}}{\partial x_{k}} = \omega_{k} \frac{\partial u_{i}}{\partial x_{k}} - \varepsilon_{ijk} \frac{1}{\rho^{2}} \frac{\partial \rho}{\partial x_{j}} \frac{\partial \tau_{kl}}{\partial x_{l}} + \frac{\varepsilon_{ijk}}{\rho} \frac{\partial^{2} \tau_{kl}}{\partial x_{j} x_{l}} - \omega_{i} \frac{\partial u_{k}}{\partial x_{k}} + \frac{\varepsilon_{ijk}}{\rho^{2}} \frac{\partial \rho}{\partial x_{j}} \frac{\partial \rho}{\partial x_{k}}.$$
(5)

Equation (5) represents the vorticity transport equation for the RANS averaged velocities, illustrating the evolution of vorticity within a fluid flow. This equation is derived from the modeled momentum equation and features effective viscosities. It showcases various contributing factors influencing the vorticity field and consequent alterations in the velocity field. In order to analyze the impact of different mechanisms on the strength of the vorticity field and its influence on velocity changes, the enstrophy equation is derived from the vorticity transport equation. The enstrophy equation, derived by multiplying both sides of the vorticity transport equation by vorticity ω_b is expressed as follows:³⁵

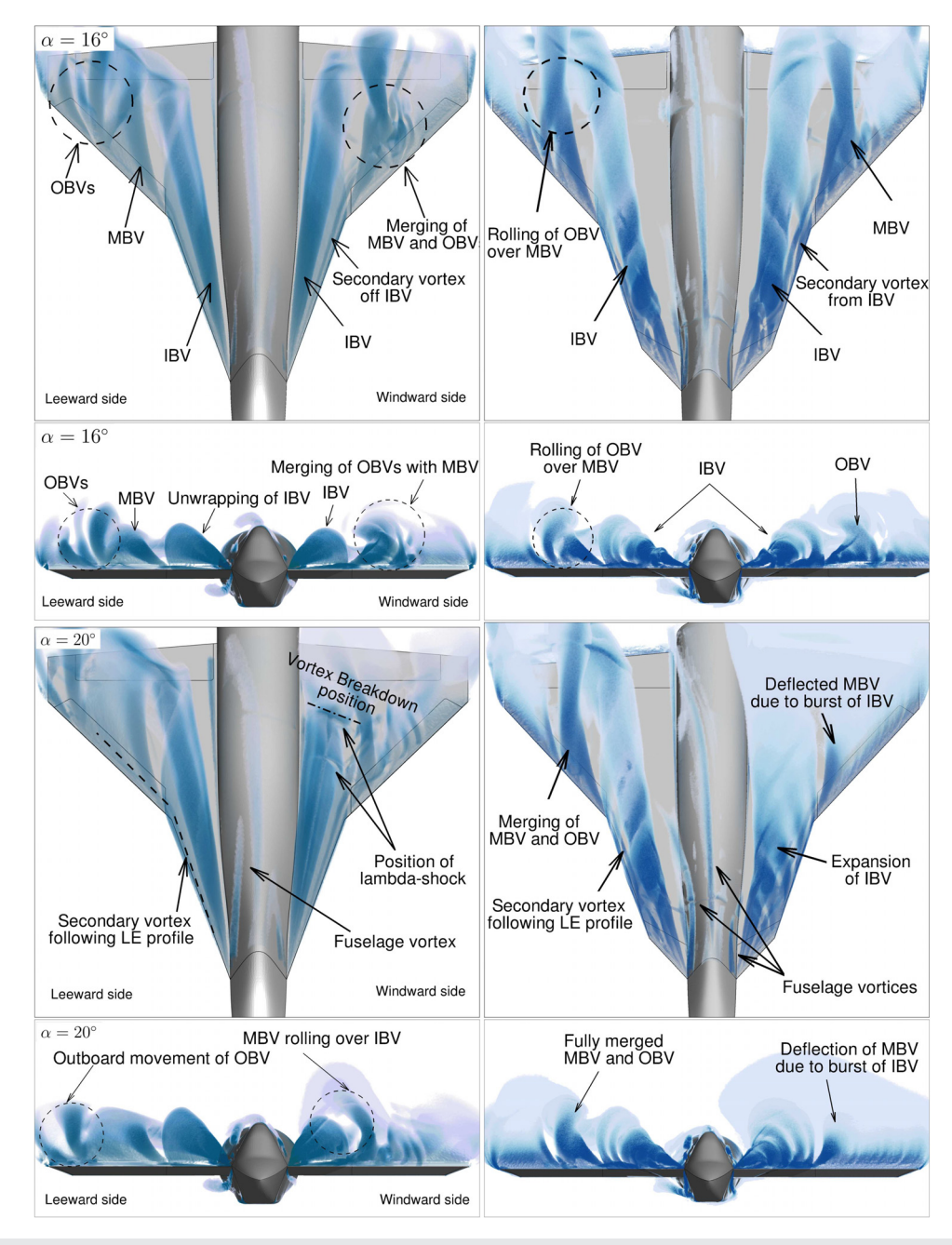


FIG. 6. Vortex system at $\alpha=16^{\circ}$ and 20° observed through volume visualization of Q in DW1 (left) and DW2 (right) at $Ma_{\infty}=0.85$ and $Re=12.53\times10^{6}$ with $AoS=5^{\circ}$ using $k-\omega$ SST model.

$$\frac{\partial \Omega}{\partial t} + u_k \frac{\partial \Omega}{\partial x_k} = \underbrace{\omega_i \omega_k \frac{\partial u_i}{\partial x_k}}_{T1} - \underbrace{\varepsilon_{ijk} \omega_i \frac{1}{\rho^2} \frac{\partial \rho}{\partial x_j} \frac{\partial \tau_{kl}}{\partial x_l}}_{T2} + \underbrace{\varepsilon_{ijk} \omega_i \frac{\partial^2 \tau_{kl}}{\rho \frac{\partial \rho}{\partial x_j} \partial x_l}}_{T3} - \underbrace{-2 \frac{\partial u_k}{\partial x_k} \Omega}_{T4} + \underbrace{\varepsilon_{ijk} \frac{\omega_i}{\rho^2} \frac{\partial \rho}{\partial x_j} \frac{\partial \rho}{\partial x_k}}_{T5}.$$
(6)

Equation (6) describes the enstrophy transport equation for the RANS averaged velocities. The temporal derivative term on the left-hand side represents the local rate of change of enstrophy with respect to time. In contrast, the spatial derivative term represents the advection of enstrophy by the velocity field. The terms on the right-hand side represent the changes of enstrophy due to production from vortex stretching due to flow gradients (T1). T2 represents the cross product of two vectors, the vorticity and the viscosity torque. T3 represents the joint

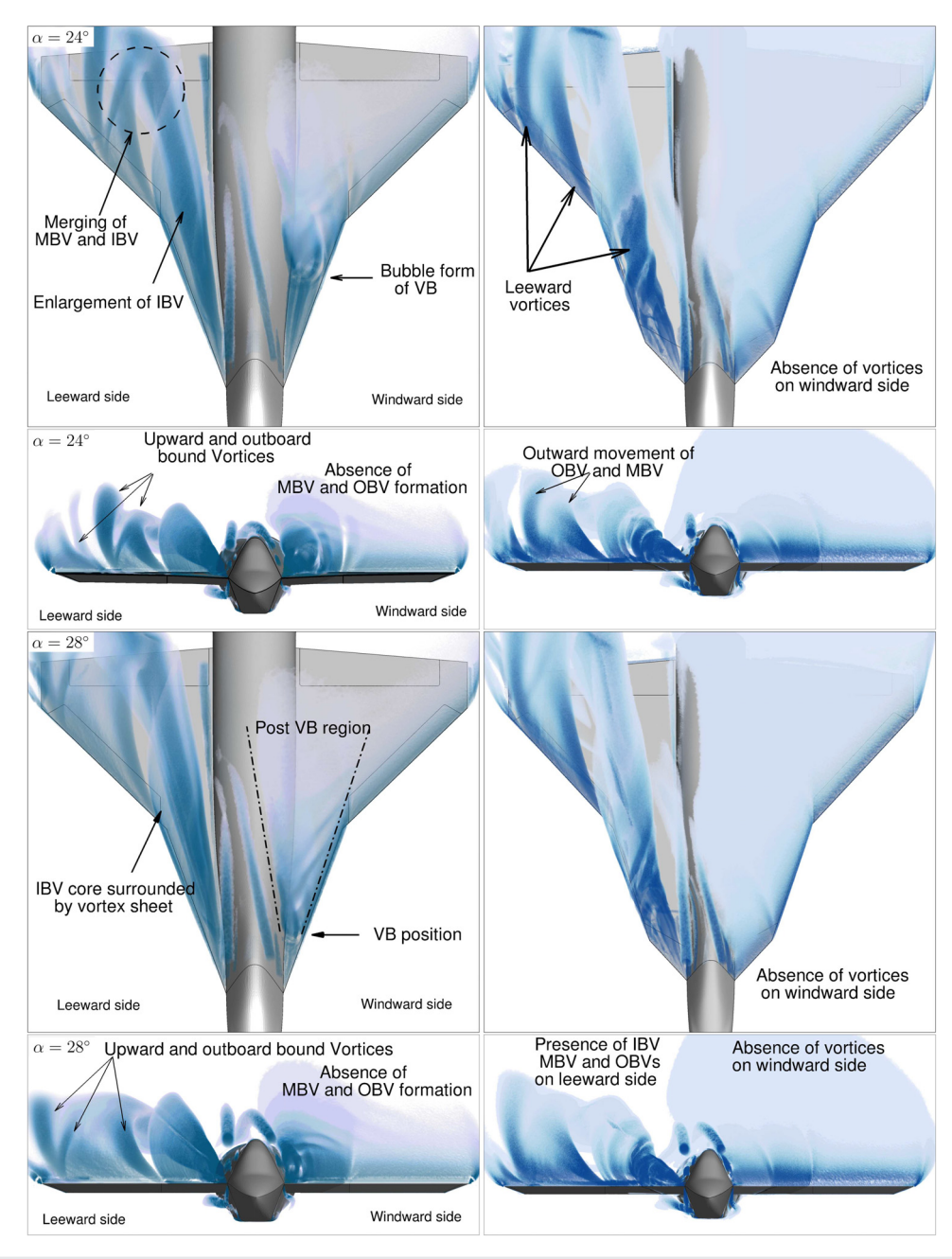


FIG. 7. Vortex system at $\alpha=24^{\circ}$ and 28° observed through volume visualization of Q in DW1 (left) and DW2 (right) at $Ma_{\infty}=0.85$ and $Re=12.53\times10^{6}$ with $AoS=5^{\circ}$ using $k-\omega$ SST model.

influence of molecular diffusion and dissipation. T4 contributes to enstrophy dissipation by accounting for the impact of dilatation. Meanwhile, T5 represents the baroclinic torque resulting from the misalignment between pressure and density gradients.

Figure 8 illustrates enstrophy and its various contributing components in DW1 at $\alpha=16^\circ$ and $\alpha=20^\circ$ at equidistant chord-wise slices. Among the transport terms shown on the right-hand side of Eq. (6),

T2 and T3 contribute the least and thus aren't shown. The T1 contour values are displayed alongside the streamlines, depicting the regions with the most negative T1 values. This indicates that at angles of $\alpha=16^\circ$ and $\alpha=20^\circ$, the secondary vortices and MBV effectively dissipate enstrophy through vortex stretching on the windward side.

However, there is a difference between the two incidence cases on the leeward side. $\alpha=20^\circ$ features significant destruction due to the

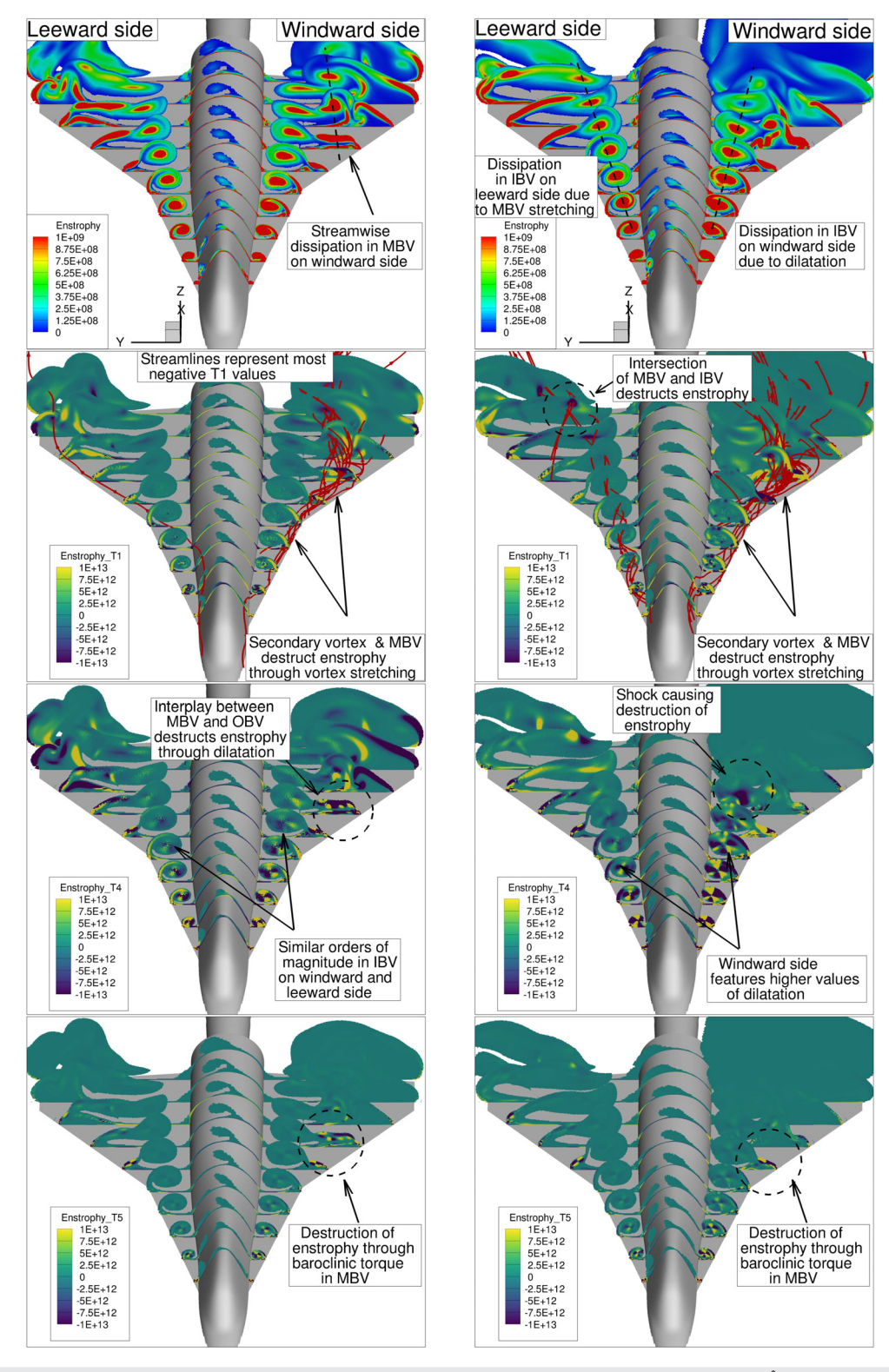


FIG. 8. Enstrophy transport terms for $\alpha=16^\circ$ (left) and $\alpha=20^\circ$ (right) with $\beta=5^\circ$ in DW1 at $Ma_\infty=0.85$ and $Re_\infty=12.53\times10^6$ with $AoS=5^\circ$ using the $k-\omega$ SST model.

intersection of MBV and IBV, whereas $\alpha=16^\circ$ shows no such effect. At $\alpha=16^\circ$, the magnitude of T4 observed in the IBV is similar on both sides of the wing. However, the interaction between MBV and OBV on the windward side shows high negative values marked by a dotted circle. It indicates that MBV and OBV reduce vorticity strength through a dilatation process.

At $\alpha=20^\circ$ on the windward side, a shock causes the breakdown of the vortex, shown by the most negative values in T4 marked by a dotted circle. Baroclinic effects are observed on the MBV on the windward side for both incidence angles.

Figure 9 shows the trajectories of IBV and MBV for the planforms at $\alpha=20^\circ$, identified from the maximum x-vorticity. In the DW2 planform, on the windward side, the IBV starts to develop close to the fuselage, undergoing deformation due to the shock that significantly deteriorates the vortex strength. Meanwhile, the MBV starts from the third-leading edge. Downstream of the deformation, the unstable vortex could still be fed by the shear layer from the second leading edge, evident from the suction footprint on the surface (marked by the circle in Fig. 9). On the leeward side, the IBV develops close to the fuselage and continues until merging with the MBV.

For DW1, on the windward side, the IBV continues to grow stronger with downstream convection of the vortex. Vortex breakdown is characterized by a sudden drop of streamwise velocity on the vortex-core axis before merging can take place. On the leeward side, the merging of IBV and MBV happens on both planforms, although the spiraling of IBV over MBV is more evident in DW2.

For both planforms, one can observe the breakdown position at $\alpha=20^{\circ}$. The breakdown of the vortex is further downstream in the case of DW1 than in DW2. Due to a greater span in DW2, the vortex has more room to propagate spanwise than in DW1, where the

spanwise cross-flow is limited between the fuselage and the leading edge. This makes the IBV more compact in DW1, whereas an unstable IBV forms at DW2. This leads to less swirl strength of the vortex, making it less susceptible to vortex breakdown in DW1. Consequently, the shock occurs delayed due to the stronger vortex development.

The position of vortex breakdown is determined by the balance between vorticity strength and shock strength.³⁶ Figure 10 shows the *x*-vorticity and *y*-vorticity in the plane of the vortex core for both planforms. In both planforms, vortex breakdown is characterized by a vortex-core expansion. The shock on DW2 distorts the vortex axis, triggering vortex breakdown due to this distortion. As expected, the shock effect on *y*-vorticity is stronger than on *x*-vorticity, causing significant changes in the pre-and post-shock regions.

D. Investigation of shock-vortex interaction

Figure 11 shows the occurrence of shocks at $\alpha=16^\circ$ and 20° for DW1 and DW2. At $\alpha=16^\circ$ in DW1, normal shocks are present in the rear section of the wing. The shock is observed to interact with the vortex system, which, however, does not exhibit any breakdown. A portion of this shock, interacting with the MBV, is responsible for the dilatation and baroclinic effects observed in Fig. 8.

In DW2, two normal shocks are produced due to the geometry, one in the front portion of the wing caused by the kink in the planform, and the other in the rear portion of the wing. In the shock near the front portion of the wing, the shock protrudes toward the front due to the higher local vorticity and axial velocity in the vortex core.

At $\alpha=20^\circ$, a fundamental difference exists in the shock-vortex interaction between DW1 and DW2. In DW1, there is a highly dynamic interaction between vortex breakdown and the shock,

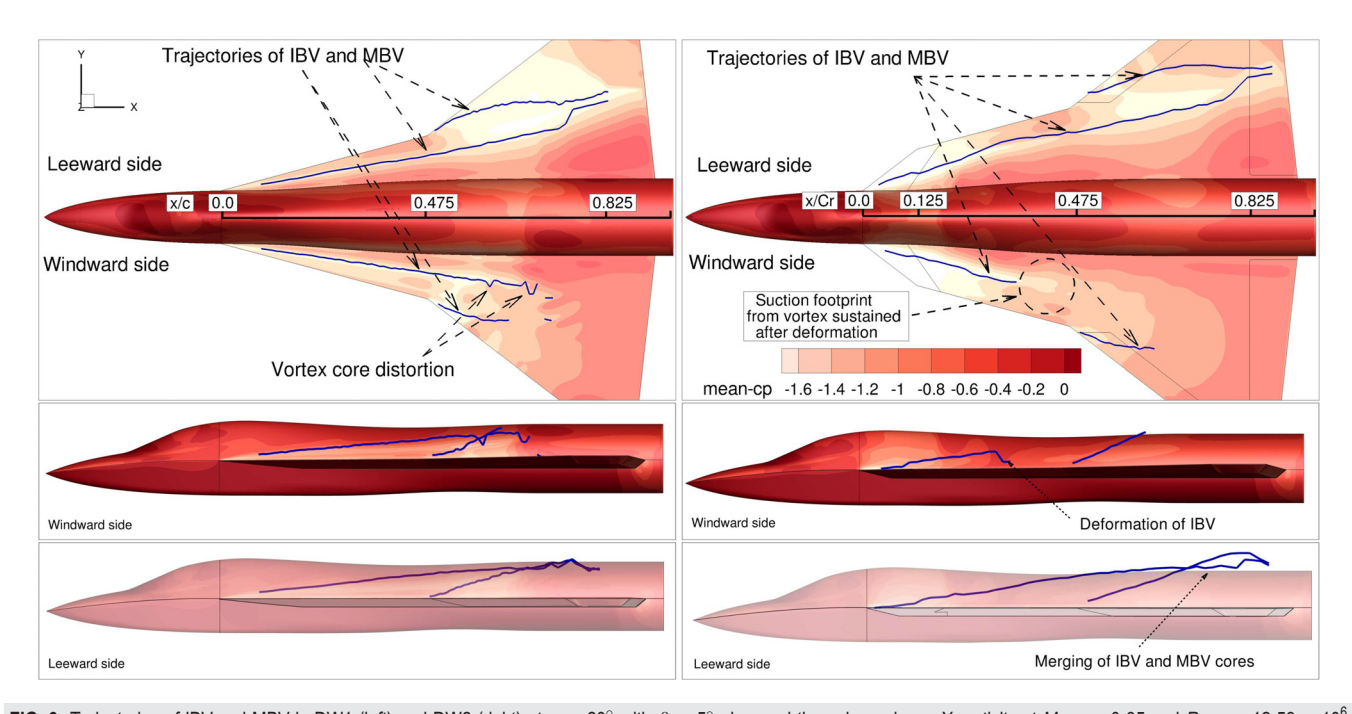


FIG. 9. Trajectories of IBV and MBV in DW1 (left) and DW2 (right) at $\alpha=20^\circ$ with $\beta=5^\circ$ observed through maximum X-vorticity at $Ma_\infty=0.85$ and $Re_\infty=12.53\times10^6$ with $AoS=5^\circ$ using $k-\omega$ SST model.

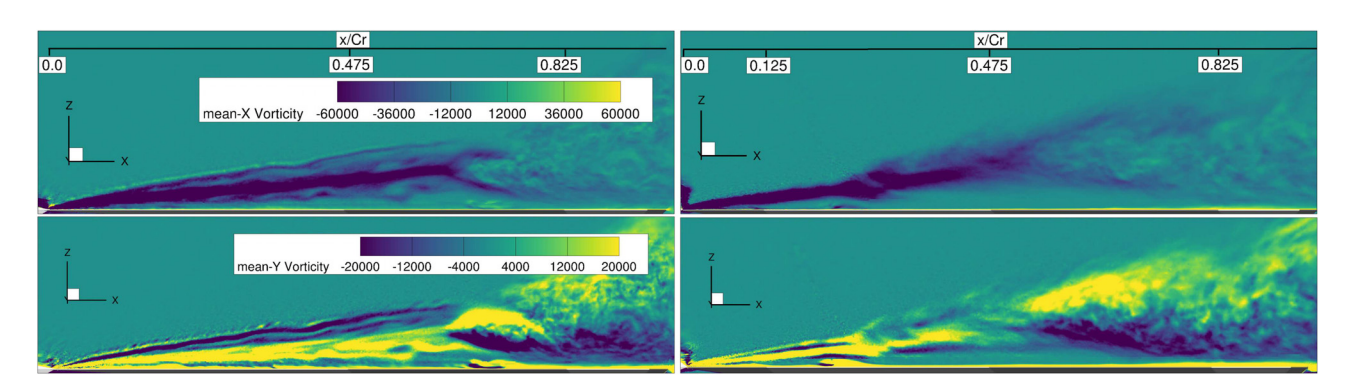


FIG. 10. Mean x and y vorticity at $\alpha=20^\circ$ with $\beta=5^\circ$ in DW1 (left) and DW2 (right) at $Ma_\infty=0.85$ and $Re_\infty=12.53\times10^6$ with $AoS=5^\circ$ using the $k-\omega$ SST model.

whereas the shock at DW2 is produced due to the kink, as observed at $\alpha=16^\circ$. To understand the transient nature in DW1, this case has been investigated with the SAS model.

Figure 12 presents a visual representation of the lambda-shock phenomenon observed over DW1 at $\alpha = 20^{\circ}$. After reaching supersonic conditions over the wing, a normal shock A is created above a

certain distance from the vortex region. However, close to the surface of the wing, where the IBV interacts with the normal shock, the shock bulges upstream and manifests as an oblique shock B within the bulged portion of the shockwave. A similar bulging of a normal shock near the vortex core was observed in Ref. 36, which numerically investigates the interaction of a longitudinal vortex with a shock wave.

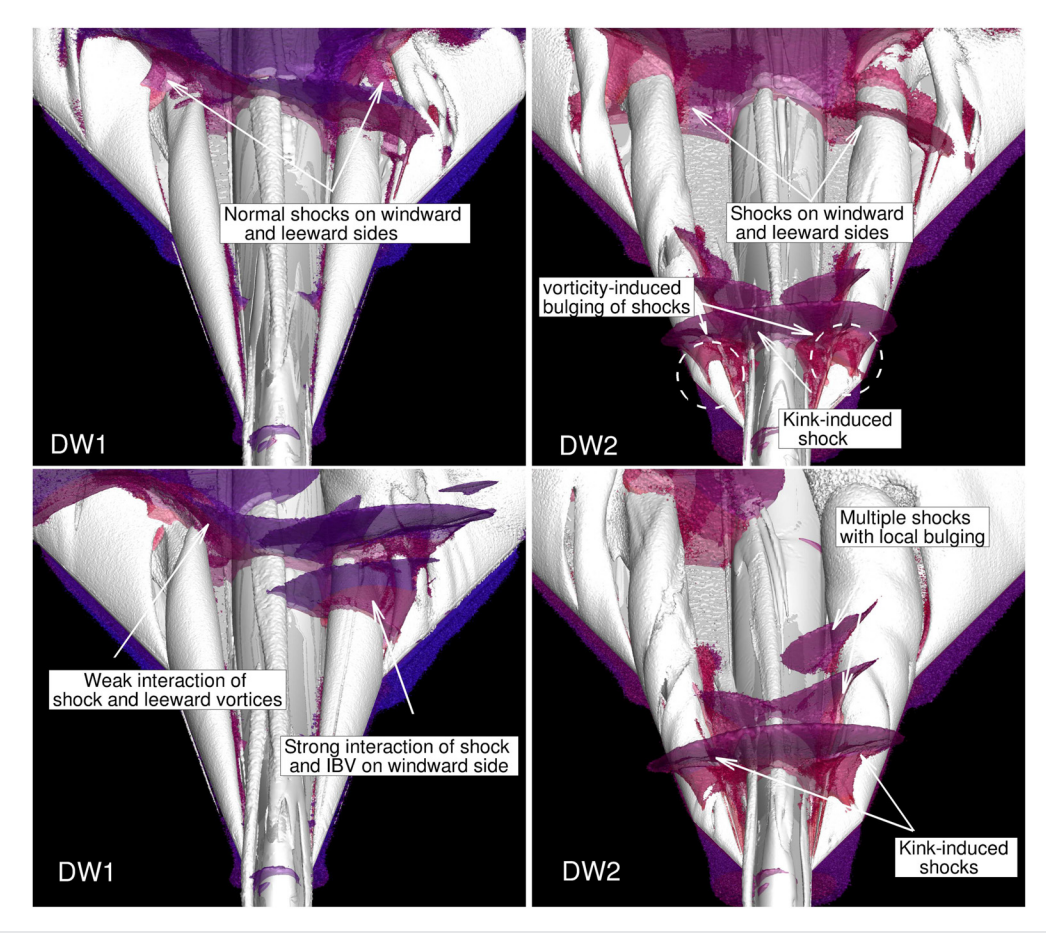


FIG. 11. DW1 and DW2 vortex-shock interaction at $\alpha=16^\circ$ (top) and 20° (bottom) observed by iso-surface $\frac{\partial \rho}{\partial x}$ and Q-Criterion at $Ma_\infty=0.85$ and $Re_\infty=12.53\times10^6$ with $AoS=5^\circ$ using the $k-\omega$ SST model.

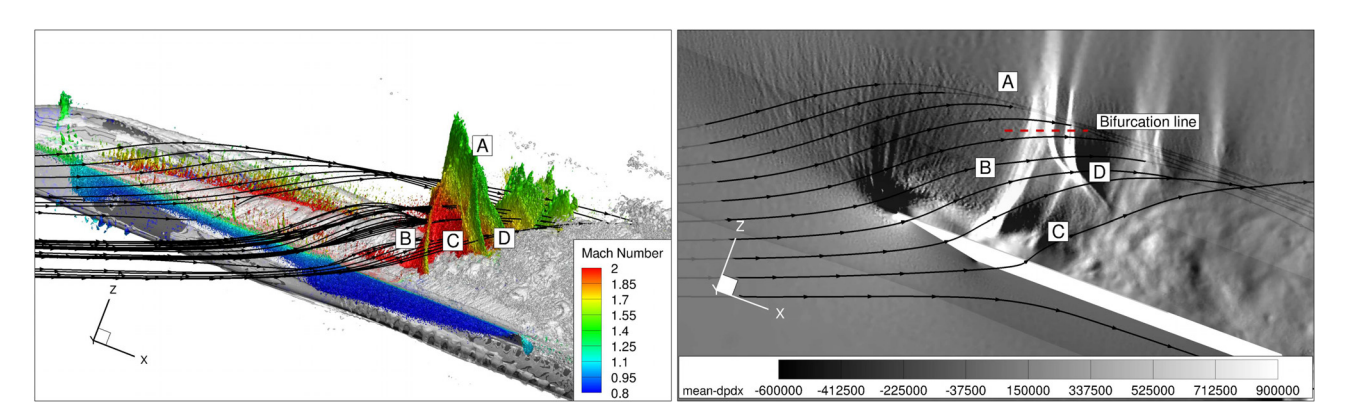


FIG. 12. 3D visualization of the lambda-shock: Iso-surface from density gradient colored by Ma (left) and visualization of the Lambda-shock by pressure gradient on a slice plane normal to span (right) in DW1 at $Ma_{\infty}=0.85$ and $Re_{\infty}=12.53\times10^6$ with $AoS=5^{\circ}$ using the $k-\omega$ SST model.

Unlike normal shocks, oblique shock B does not immediately bring the supersonic flow state back to a subsonic state. Instead, it alters the flow's direction while retaining its supersonic state. The shock D finally brings the flow back to a subsonic state. A weak shock C exists in the supersonic regime between shocks B and D.

Figure 12 represents the observed lambda-shock at an inclined plane aligned parallel to the local flow velocity. The visualization plane has been chosen to observe the lambda shock, which interacts with the vortex core of the IBV.

It has been observed that the shock system exhibits a buffet mechanism with an oscillation frequency of around 120 Hz. Figure 13 shows the quasi-periodic oscillation of C_{my} for over 25 cycles due to shock-buffet over the wing. During the buffet, the shock oscillates between the chord positions $x/C_r=0.4$ and 0.5. Selected flow states of the oscillation are shown in Fig. 14 to illustrate the evolution of the lambda-shock, with the corresponding instances marked in Fig. 13.

One can observe a multitude of shocks over the wing. At state 1, a normal shock is created, recovering the flow to a subsonic state. At state 2, as the normal shock moves downstream, it weakens, characterized by higher downstream velocity than state 1. At state 3, this normal shock undergoes bifurcation, indicating the creation of an oblique shock. Also at this state, the shock-affected boundary layer starts to shed vortices downstream close to the wing's surface.

At state 4, multiple weak shocks can be observed in the supersonic region. Until state 6, the shedding of shock-induced boundary

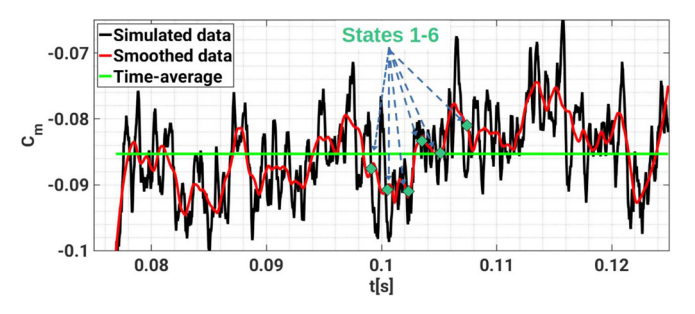


FIG. 13. Quasi-periodic oscillation of C_{my} at $\alpha=20^\circ$ and $\beta=5^\circ$ in DW1 at $Ma_\infty=0.85$ and $Re_\infty=12.53\times10^6$ with $AoS=5^\circ$ using the SAS model.

layer vortices leads to the high-frequency oscillation of the lambdashock, whose lifetime is longer than the low-frequency buffet of the normal shock prior to the formation of the lambda-shock in-state 1.

It needs to be noted that the shock-induced boundary layer vortices appear from state 3 onward, indicating that the lambda shock causes them. Additionally, the transient aspect of the VB indicates that the lambda-shock could adapt to the VB's dynamics, leading to its buffeting. We note that the shock triggers the breakdown of IBV, yet the shifting position of the VB induces an adjustment in the shock, causing a buffeting mechanism. Notably, this phenomenon is absent in DW2.

In an extensive examination conducted by Deléry, 37 the study illustrates the relevance of various parameters in the context of vortex breakdown caused by the interaction of shockwaves and vortices. These parameters include the swirl velocity and the axial velocity of the vortex core. Deléry suggests that the swirl ratio or the Rossby number could indicate the vortex's intensity and, consequently, its susceptibility to shock-induced breakdown. The Rossby number, a dimensionless parameter, is the ratio of the axial and circumferential momentum within a vortex. This investigation employs both the maximum axial velocity at the vortex core, denoted as U_{axiab} and the simplified maximum in-plane y-velocity, denoted as U_{Ymax} , of the vortex. The relation defines the Rossby number as

$$Ro = \frac{U_{axial}}{U_{Ymax}}. (7)$$

When a vortex encounters a normal shock, the swirl velocity remains relatively constant, while the axial velocity decreases, decreasing the Rossby number. It corresponds to an increase in vortex intensity, consequently raising the susceptibility of the vortex to breakdown. Researchers, such as Spall *et al.* and Robinson *et al.* have explored using the Rossby number as a criterion for breakdown. They have applied this criterion to computational data from flow around slender delta wings and found that the critical Rossby number falls between 0.9 and 1.4 in most cases. A stable vortex core is typically observed for Rossby numbers above 1.4. The Rossby number was computed to address this specific criterion.

Figure 15 shows the distribution of Rossby numbers for the IBV in DW1 and DW2. On the leeward side, where the shock has a comparatively weak influence on axial velocity, the Rossby number

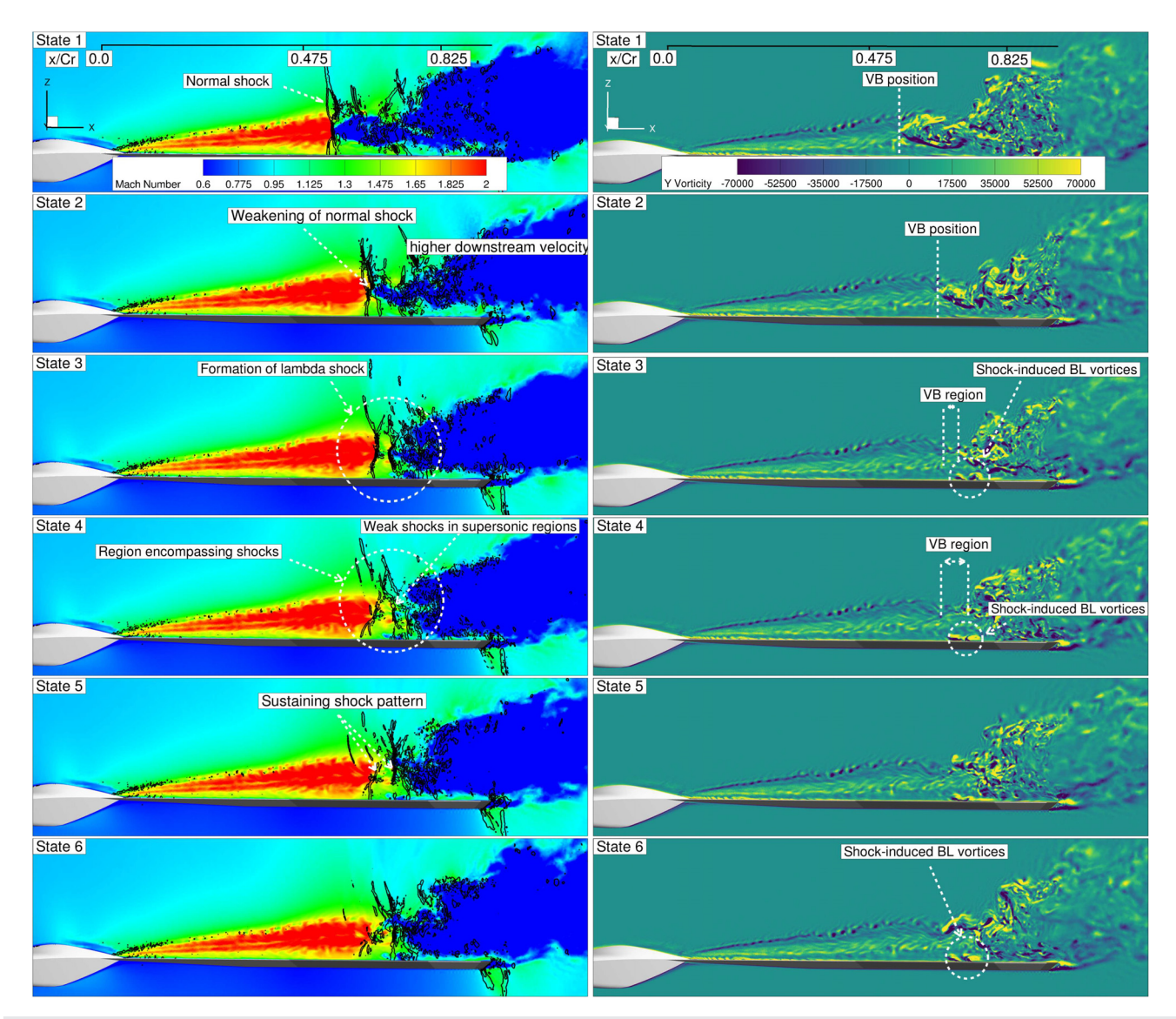


FIG. 14. Evolution of lambda-shock and vortex unsteadiness observed through quasi-periodic states of shock buffet using Ma contours and dp/dx iso-lines (left) and Y - vortic-ity (right) at $\alpha = 20^\circ$ and $\beta = 5^\circ$ in DW1 at $\textit{Ma}_\infty = 0.85$ and $\textit{Re}_\infty = 12.53 \times 10^6$ with $\textit{AoS} = 5^\circ$ using the SAS model.

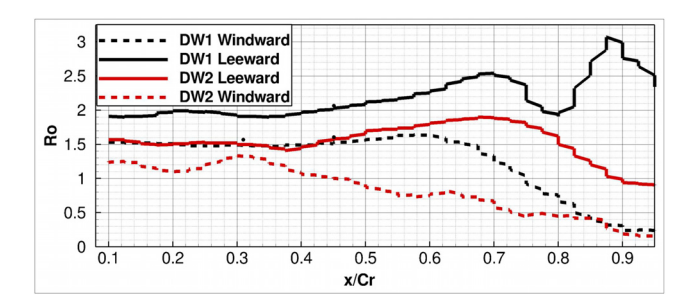


FIG. 15. Rossby number of IBV in DW1 and DW2 at $\alpha=20^\circ$ and $\beta=5^\circ$ at $Ma_\infty=0.85$ and $Re_\infty=12.53\times10^6$ with $AoS=5^\circ$ using the $k-\omega$ SST model.

remains at elevated levels, indicating a stable range. Consequently, the vortex displays a relatively low susceptibility to disturbances. In contrast, the shock system significantly affects axial velocity on the windward side, resulting in a pronounced reduction of the Rossby number. It, in turn, amplifies the susceptibility of the vortex to breakdown.

IV. CONCLUSION

This article presents a comprehensive numerical study of doubleand triple-delta wing planforms under transonic flow conditions. The simulations accurately predict the lift, with the pitching moment being more sensitive to the location of vortex breakdown. It underscores the challenges in precisely capturing vortex breakdown in transonic flow conditions. The vortex topology of the planforms under different angles of attack has been observed. On the double-delta wing, at a low incidence angle of 16° , the IBV and MBV develop and sustain the shock without breaking down due to very strong concentrated vortex development. At higher incidence angles of 20° , strong interaction between the IBV and MBV on the windward side and the shock leads to subsequent breakdown. At this incidence angle, the triple-delta wing features a shock, causing IBV to break upstream due to its less stable character.

The enstrophy analysis of the DW1 planform at angles of attack $\alpha=16^\circ$ and $\alpha=20^\circ$ reveals distinct characteristics in vortex dynamics. At $\alpha=16^\circ$, the interaction between the secondary vortices and MBV dissipates enstrophy through vortex stretching on the windward side, with minimal impact on the leeward side. Conversely, at $\alpha=20^\circ$, significant destruction occurs on the leeward side due to the intersection of MBV and IBV. The dilatation process, mainly observed through the dilation term of the enstrophy transport equation, highlights the reduction of vorticity strength in the MBV and OBV on the windward side. Additionally, at $\alpha=20^\circ$, the shock induces vortex breakdown primarily in the MBV on the windward side, and baroclinic effects are observed in the MBV on the windward side for both incidence angles.

Furthermore, a fundamental difference has been observed for the first time in this study between DW1 and DW2 configurations in their response to vortex breakdown and shock buffet at $\alpha=20^{\circ}$. The analysis highlights that the double-delta wing undergoes shock-induced vortex breakdown, and the transient nature of this breakdown prompts adjustments in the shock position, resulting in a shock buffet. Conversely, the breakdown in the triple-delta wing is associated with a stationary shock induced by the kink in the planform. The SAS model reveals a quasiperiodic oscillation of the pitching moment, offering a detailed visualization of the lambda-shock evolution. This observation unveils the causal relationship between shock buffet and vortex breakdown. Examining the dilatation term in the enstrophy transport equation clarifies that the lambda-shock serves as the driving force behind vortex breakdown in the double-delta wing. These findings underscore the intricate interplay between shock-induced effects and vortex dynamics, shedding light on the complex aerodynamic behavior of the planforms.

ACKNOWLEDGMENTS

The authors gratefully acknowledge the financial support provided by Airbus Defence and Space (ADS) for the project "Analysis of Unsteady Effects in Fighter Aircraft Aerodynamics." The contributions of the German Aerospace Center (DLR) in providing the TAU code and Ennova Technologies for the meshing software are sincerely appreciated. Additionally, the authors extend their gratitude to the Gauss Centre for Supercomputing for granting access to the necessary computing hours for this study.

AUTHOR DECLARATIONS Conflict of Interest

The authors have no conflicts to disclose.

Author Contributions

K. Rajkumar: Investigation (equal); Methodology (equal); Resources (equal); Software (equal); Validation (equal); Visualization (equal);

Writing – original draft (equal). **T. Di Fabbio:** Writing – review & editing (equal). **E. Tangermann:** Supervision (equal); Writing – review & editing (equal). **M. Klein:** Funding acquisition (equal); Supervision (equal); Writing – review & editing (equal).

DATA AVAILABILITY

The data that support the findings of this study are available from the corresponding author upon reasonable request.

REFERENCES

- ¹S. M. Hitzel, "Challenges and needs for the understanding of combat aircraft aerodynamics," No. STO-MP-AVT-307-19, 2019.
- ²N. C. Lambourne and D. W. Bryer, "The bursting of leading-edge vortices some observations and discussion of the phenomenon," Report No. 3282 (Aeronautical Research Council. 1962).
- ³J. R. Chambers and S. B. Grafton, "Aerodynamic characteristics of airplanes at high angles of attack," Report No. NASA-TN-74097, 1977.
- ⁴J. R. Chambers and E. L. Analin, "Analysis of lateral-directional stability characteristics of a twin-jet fighter airplane at high angles of attack," Report No. NASA-TN-D-5361, 1969.
- ⁵L. A. Schiavetta, O. J. Boelens, S. Crippa, R. M. Cummings, W. Fritz, and K. J. Badcock, "Shock effects on delta wing vortex breakdown," J. Aircr. **46**, 903–914 (2009)
- 61. Gursul, "Review of unsteady vortex flows over slender delta wings," J. Aircr. 42, 299–319 (2005).
- ⁷D. H. Peckham and S. A. Atkinson, Preliminary Results of Low Speed Wind Tunnel Tests on a Gothic Wing of Aspect Ratio 1.0 (Aeronautical Research Council, 1960), pp. 1–38.
- ⁸D. L. Darmofal and E. M. Murman, "On the trapped wave nature of axisymmetric vortex breakdown," AIAA Paper No. 1994-2318, 1994.
- ⁹A. M. Mitchell and J. Délery, "Research into vortex breakdown control," Prog. Aerosp. Sci. 37, 385–418 (2001).
- 10 Z. Rusak and D. Lamb, "Prediction of vortex breakdown in leading-edge vortices above slender delta wings," J. Aircr. 36, 659–667 (1999).
- ¹¹M. Jones, A. Hashimoto, and Y. Nakamura, "Criteria for vortex breakdown above high-sweep delta wings," AIAA J. 47, 2306–2320 (2009).
- ¹²S. Pfnür, A. Hövelmann, D. Sedlacek, and C. Breitsamter, "Vortex flow interaction phenomena on multi swept delta wings at subsonic speeds," NATO Report No. 1STO-MP-AVT-307, 2019, pp. 1–23.
- ¹³S. Hitzel, "Status of vortex interaction on combat aircraft-physics understood, simulation tool demands, quality and cost," AIAA Paper No. 2022-0159, 2022.
- 14S. Hitzel, "Combat aircraft vortex interaction-design, physics and CFD-tools," AIAA Paper No. 2022-0156, 2022.
- 15 A. Hövelmann, A. Winkler, S. M. Hitzel, K. Richter, and M. Werner, "Analysis of vortex flow phenomena on generic delta wing planforms at transonic speeds," in *New Results in Numerical and Experimental Fluid Mechanics XII* (Springer, 2020), pp. 307–316.
- ¹⁶S. Hitzel, A. Winkler, and A. Hövelmann, "Vortex flow aerodynamic challenges in the design space for future fighter aircraft," in *New Results in Numerical and Experimental Fluid Mechanics XII* (Springer International Publishing, 2020), pp. 207-306.
- pp. 297–306.

 17 A. Schütte and R. N. Marini, "Computational aerodynamic sensitivity studies for generic delta wing planforms," in *New Results in Numerical and Experimental Fluid Mechanics XII* (Springer International Publishing, 2020), pp. 338–348.
- 187. Solution and C. Breitsamter, "Leading-edge vortex interactions at a generic multiple swept-wing aircraft configuration," J. Aircr. 56, 2093–2107 (2019).
- ¹⁹T. Di Fabbio, K. Rajkumar, E. Tangermann, and M. Klein, "Towards the understanding of vortex breakdown for improved RANS turbulence modeling," Aerosp. Sci. Technol. 146, 108973 (2024).
- ²⁰T. Di Fabbio, E. Tangermann, and M. Klein, "Investigation of transonic aero-dynamics on a triple-delta wing in side slip conditions," CEAS Aeronaut. J. 13, 453–470 (2022).

- ²¹S. Langer, A. Schwöppe, and N. Kroll, "The DLR flow solver TAU—Status and recent algorithmic developments," AIAA Paper No. 2014-0080, 2014.
- ²²F. R. Menter, "Two-equation eddy-viscosity turbulence models for engineering applications," AIAA J. 32, 1598–1605 (1994).
- ²³F. R. Menter and Y. Egorov, "The scale-adaptive simulation method for unsteady turbulent flow predictions. Part 1: Theory and model description," Flow. Turbul. Combust. 85, 113–138 (2010).
- ²⁴J. C. Kok, "A high-order low-dispersion symmetry-preserving finite-volume method for compressible flow on curvilinear grids," J. Comput. Phys. 228, 6811–6832 (2009).
- 25A. Jameson, W. Schmidt, and E. Turkel, "Numerical solution of the Euler equations by finite volume methods using Runge Kutta time stepping schemes," AIAA Paper No. 1981-1259, 1981.
- 26M. Galle, T. Gerhold, and J. Evans, "Parallel computation of turbulent flows around complex geometries on hybrid grids with the DLR-TAU code," in 11th Parallel CFD Conference (1999).
- 27W. Sutherland, "The viscosity of gases and molecular force," London, Edinburgh, Dublin Philos. Mag. J. Sci. 36, 507-531 (1893).
- ²⁸F. Goetten, D. F. Finger, M. Marino, C. Bil, M. Havermann, and C. Braun, "A review of guidelines and best practices for subsonic aerodynamic simulations using RANS CFD," in APISAT 2019 Asia Pacific International Symposium on Aerospace Technology (Engineers Australia, 2019), pp. 227–245.
- ²⁹N. Georgiadis, J. Dudek, and T. Tierney, "Grid resolution and turbulent inflow boundary condition recommendations for NPARC calculations," AIAA Paper No. 95-2613, 1995.

- ³⁰G. Siouris, Aerodynamic Forces and Coefficients (Springer, New York, 2004), pp. 53–154.
- 31 A. Krumbein, V. Togiti, and A. Schütte, "Improvement of physical modeling for vortex-dominated flows," Report No. AFRL-AFOSR-UK-TR-2022-0019, 2018.
- ³²B. Y. Zhou, B. Diskin, N. R. Gauger, J. K. Pardue, A. Chernikov, C. Tsolakis, F. Drakopoulos, and N. N. Chrisochoides, "Hybrid RANS/LES simulation of vortex breakdown over a Delta wing," AIAA Paper No. 2019-3524, 2019.
- ³³T. Landa, L. Klug, R. Radespiel, S. Probst, and T. Knopp, "Experimental and numerical analysis of a streamwise vortex downstream of a delta wing," AIAA J. 58, 2857–2868 (2020).
- ³⁴T. Di Fabbio, E. Tangermann, and M. Klein, "Analysis of the vortex-dominated flow field over a delta wing at transonic speed," Aeronaut. J. 127, 1851–1868 (2023).
- 35A. N. Lipatnikov, S. Nishiki, and T. Hasegawa, "A direct numerical simulation study of vorticity transformation in weakly turbulent premixed flames," Phys. Fluids 26, 105104 (2014).
- ³⁶G. Erlebacher, M. Y. Hussaini, and C. W. Shu, "Interaction of a shock with a longitudinal vortex," J. Fluid Mech. 337, 129–153 (1997).
- ³⁷J. M. Delery, "Aspects of vortex breakdown," Prog. Aerosp. Sci. 30, 1–59 (1994).
- ⁵⁸I. M. Kalkhoran and M. K. Smart, "Aspects of shock wave-induced vortex breakdown," Prog. Aerosp. Sci. 36, 63–95 (2000).
- ³⁹R. E. Spall, T. B. Gatski, and C. E. Grosch, "A criterion for vortex breakdown," Phys. Fluids 30, 3434–3440 (1987).
- ⁴⁰B. A. Robinson, R. M. Barnett, and S. Agrawal, "Simple numerical criterion for vortex breakdown," AIAA J. 32, 116–122 (1994).